

Mechanistic Insight into Hydrogen-Assisted Carbon Dioxide Reduction with Ilmenite

Zhuo Cheng,^{*,†} Deven S. Baser,[†] Vedant Shah, Jonathan A. Fan, and Liang-Shih Fan



Cite This: <https://dx.doi.org/10.1021/acs.energyfuels.0c03214>



Read Online

ACCESS |



Metrics & More



Article Recommendations

ABSTRACT: The transformation of CO₂ to chemicals and fuels offers a means of CO₂ utilization while mitigating the global carbon footprint. An attractive strategy involves the CO₂ reforming of methane with oxygen carriers. In this strategy, methane is used as the reducing agent to provide hydrogen for CO₂ reduction. This study aims to investigate the reactivity of the ilmenite-based oxygen carrier undergoing a redox reaction for CO₂ reduction coupled with methane reforming and the underlying mechanism using combined experimental study and density functional theory calculations. The enhanced activity for the methane conversion and CO₂ reduction with FeTiO₃ was revealed under the CH₄/CO₂ ratio of >8.75 with CO₂ conversion of >95%. The mechanistic probe indicated that the oxygen vacancies and hydrogen atoms from the successive dissociation of CH₄ are crucial for CO₂ activation and reduction. In the dominant formate pathway, the CO₂ molecule is hydrogenated to the HCOO* intermediate species and then decomposes to CO via the C–O and C–H cleavage at the oxygen vacancy site with a low barrier of 62.5 kJ/mol. These results shed light on the fundamental understanding of hydrogen-assisted CO₂ reduction over ilmenite-based oxygen carriers and open up future research on potential strategies to improve CO₂ utilization for redox reactions.

1. INTRODUCTION

CO₂ emissions, primarily from the combustion of fossil fuels, have continued to steadily increase over the past decade.^{1–3} There has been much effort to develop efficient approaches for CO₂ capture or conversion.^{3–8} The CO₂ conversion to value-added chemicals is a solution that is widely considered to both address the concerns over the decreasing supply of fossil fuels and reduce CO₂ emissions.^{9,10} However, using CO₂ as a C₁ feedstock via direct dissociation has been challenging because its molecular structure is very stable.¹¹

Photochemical, electrochemical, biological, and thermochemical approaches have been applied for converting CO₂ into useful products, such as CO, CH₃OH, and HCOOH.^{12–14} In addition to these commodity-scale chemicals, catalytic cycloaddition of CO₂ to form cyclic carbonates has also been investigated that shows CO₂ utilization capability at low temperatures.^{15,16} Among these products, the conversion of CO₂ into CO, as a part of syngas, through the dry reforming of methane (DRM) has attracted growing attention because it can simultaneously convert CH₄ and CO₂. Typically, a noble-metal-based catalyst is used for DRM to achieve a high CH₄ conversion and a high CO₂ utilization for an extended period of time.¹⁷ However, many challenges need to be addressed before this technology can be applied. The main disadvantage of DRM is the significant production of carbon that becomes deposited on the catalyst surface. The carbon deposition impairs the activity of the catalyst in the reaction and reduces its useful life.^{18,19}

In addition to improving the catalyst activity for DRM, different configurations of this chemistry have been envisioned for improving the overall efficiency. This ranges from electrochemical CO₂ separation coupled with DRM,²⁰

“super-dry” reforming using a catalyst, an oxygen carrier, and a CO₂ sorbent²¹ to chemical looping reforming.^{6,22–24} Thermodynamics dictate that Fe-based oxygen carriers, under certain oxidation states, have the ability to reduce CO₂.^{6,25,26} Particularly, this innovative CO₂ reduction technology with the chemical looping concept has attracted much attention and been investigated recently.^{22,26–29} Chemical looping reforming of methane coupled with CO₂ reduction (CLR-CR) is a novel technology for CO and H₂ production, which is developed and established on the basis of the chemical looping partial oxidation process and CO₂ reduction process, as shown in Figure 1.

The CLR-CR technology can simultaneously convert CH₄ and CO₂ into syngas in the fuel reactor using oxygen carriers. The oxygen carrier donates oxygen from its lattice for CH₄ oxidation, leading to the reduction of the oxygen carrier with the formation of oxygen vacancies. The reduced oxygen carrier is then oxidized in the air reactor. In contrast to the conventional DRM process, the CLR-CR system can be operated autothermally, without the need for an external heat source. The CLR-CR system can also directly produce high-quality syngas (CO + H₂).^{22–24,26,27,30} The CLR-CR systems with concurrent moving bed reactors have not only shown a high CO₂ utilization capability but also the ability to

Special Issue: In Honor of Professor Michael Klein

Received: September 23, 2020

Revised: October 22, 2020

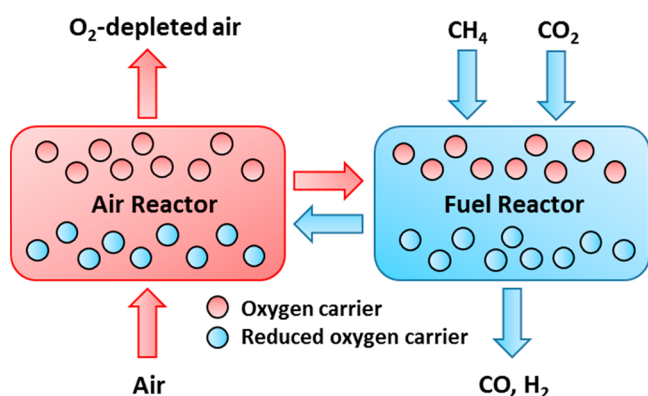


Figure 1. Schematic representation of the CLR-CR.

modularize the CLR-CR system for a higher reforming capacity with Fe–Ti composite metal oxides as oxygen carriers.^{6,31} For this system, CO₂ was used as a partial substitute to CH₄, reducing the CH₄ feed by 23% to produce the same amount of liquid fuel compared to the baseline gas to liquid technology.²² This increased CO₂ reduction is attributed to the unique interaction of CH₄, CO₂, and the ilmenite-based oxygen carrier, which has not yet been studied. For ilmenite, it was of great importance to understand the active solid phase that determines the improved CO₂ reduction and CH₄ conversion to syngas. For syngas production without CO₂, the formation of FeTiO₃ has been deemed to be the active phase that determined the quality of syngas.³² For the CLR-CR, the thermodynamic gas- and solid-phase profile across the concurrent moving bed reducer is shown in Figure 2.

At the top of the fuel reactor, MO_x is fed in with CH₄ and CO₂, where MO_x is Fe₂TiO₅. The reducer bottom that has MO_y as a product stream can be represented by reduced FeTiO₃. Figure 2 tracks the evolution of the gas phase and the solid phase as they move through the fuel reactor. As seen in Figure 2a, the gas phase transforms from CO₂ and H₂O to a low-purity syngas to a high-purity syngas, with the onset of the latter represented by the dotted line across the graphs in the gas-phase plot. Correspondingly, this can be attributed to the

FeTiO₃–Fe solid-phase transition, as seen in Figure 2b. This profile confirms the link between the high syngas purity and the reduction of FeTiO₃³² and couples its reduction with the improved CO₂ utilization as well. However, the factors determining the CO₂ utilization capability of the CLR-CR system are unclear, and the reaction mechanism for enhancing the activity of FeTiO₃ still needs to be discussed. In the present work, the reactivity of FeTiO₃ for CO₂ conversion at various CH₄/CO₂ ratios was investigated using the thermogravimetric analyzer (TGA) and differential bed reactor. Afterward, density functional theory (DFT) calculations were performed to explore the activity/structure relationship and the reaction pathway of the CLR-CR. Additionally, the phase composition of FeTiO₃ was also characterized.

2. EXPERIMENTAL SECTION

2.1. Experimental Procedure. Iron–titanium composite materials used as oxygen carriers in this study are commercial FeTiO₃, which were purchased from Sigma-Aldrich (99.9% purity, 100 mesh). The thermogravimetric tests were performed in a Setaram SETSYS Evolution TGA. These tests were run by taking 10–15 mg of FeTiO₃ powder in a crucible and subjecting it to reduction under 50% CH₄ with balance N₂. Solid conversion of FeTiO₃ is defined as stated in eq 1, which is directly correlated to the amount of oxygen donated or the reforming activity. A solid conversion of 0% represents the FeTiO₃ phase, and a solid conversion of 100% represents the Fe phase.

$$\text{solid conversion} = \frac{\text{weight change of the sample}}{(\text{weight of FeTiO}_3) \times \frac{\text{molecular weight of O}}{\text{molecular weight of FeTiO}_3}} \times 100\% \quad (1)$$

The schematic for the differential bed reactor is portrayed in previous studies.^{33,34} A ceramic reactor with 38.1 cm length and 12.7 cm internal diameter was used for this study. A heated section of 15.2 cm was obtained through external heaters by a Watlow ceramic fiber full cylinder heater. A 1 g sample of FeTiO₃ was loaded in the middle of the heated zone for all of the studies involving the differential bed reactor. This bed corresponded to 0.625 cm³ in volume, which was used to calculate the gas hourly space velocity (GHSV) of the gases. For all of the experiments, the GHSV of CH₄ was maintained at 2400 h^{−1} and the GHSV for CO₂ was varied between 240 and 2400 h^{−1}. All differential bed tests were performed at 950 °C and 1 atm. Blank runs

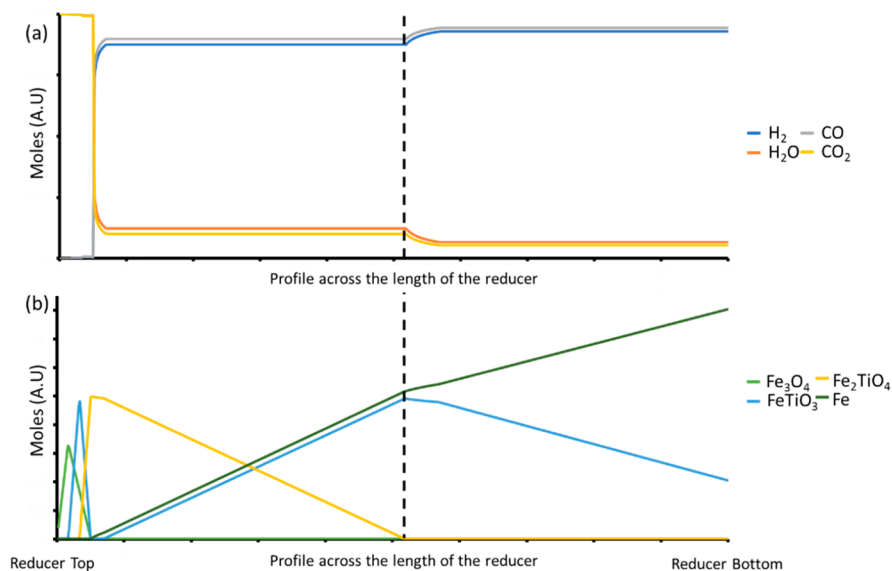


Figure 2. Profile across the length of the reducer starting from the top of the fuel reactor to the bottom for the (a) gas-phase and (b) solid-phase.

were performed for all of the experiments to account for any activity or carbon deposition as a result of the reactor. A micro-gas chromatography (micro-GC) analyzer was applied to analyze the composition of the outlet gas from the differential bed reactor. A Varian 490 micro-GC with two channels was employed for this study. The micro-GC was calibrated at three points around the gas composition expected from the outlet gas.

The X-ray diffraction (XRD) analysis was used to identify the phases of ilmenite samples as the co-feed composition was changed. For all five samples from this study, a Rigaku SmartLab X-ray diffractometer integrated with a diffracted beam monochromator was used. These scans were run between 2θ of 20 and 60 with an accelerating voltage of 40 kV and filament current of 44 mA. Raman spectroscopy was carried out on the co-feed samples to analyze the carbon deposition on the metal oxides post-reaction. A Renishaw Smiths combined Raman/infrared (IR) microprobe was used to analyze the Raman spectra of the five samples at a wavelength setting of 514 nm. The objective and gradient of 50 \times and 1800, respectively, were used for all of the samples. Mössbauer spectroscopy was used to characterize the state of Fe in the post-reaction FeTiO₃ metal oxide samples from the co-feed studies. The See Co. Mössbauer instrument with the Jains SHI-4 cryostat was used to collect this data. The instrument was calibrated with α -Fe foil (<25 mm thick) at room temperature. The spectra of each sample were collected at 4.2 K, corresponding to the boiling point of liquid He at ambient pressure. Additionally, pure FeTiO₃ spectra were also collected that gave the basis for verifying the fitting parameters.

2.2. Computational Procedure. DFT calculations were performed using the Vienna Ab Initio Simulation Package (VASP).^{35,36} Generalized gradient approximation (GGA) of Perdew, Burke, and Ernzerhof (PBE)³⁷ was adopted to represent the exchange-correlation energy. The projector-augmented wave (PAW) method^{38–40} was used to describe the wave functions of the atomic cores with a 400 eV energy cutoff. The tetrahedron method with Blöchl corrections⁴¹ was used to set the partial occupancies, and a Monkhorst–Pack k -point mesh of $6 \times 6 \times 1$ was used for surface calculations. The structures of FeTiO₃ bulk and surface were optimized until the energy converged to 1×10^{-5} eV per atom and the force converged to 0.01 eV Å⁻¹. The Hubbard U parameter was employed for self-interaction correction. U values of 5 and 1 eV were used for Fe ions and Ti ions, respectively.^{42,43}

The oxygen vacancy formation energy per vacancy was calculated using the following expression:

$$E_f = \left[\left(E_V + \frac{n}{2} E_{O_2} \right) - E_{tot} \right] / n \quad (2)$$

where E_{tot} and E_V are the total energy of the FeTiO₃ surface and the reduced surface, respectively, E_{O_2} is the energy of isolated O₂, and n is the number of oxygen vacancies.

The adsorption energy of the adsorbate (E_{ad}) is the total energy difference between before and after the molecular adsorption at each surface

$$E_{ad} = E_A + E_{surf} - E_{(A+surf)} \quad (3)$$

where E_{surf} is the total energy of the clean FeTiO₃ surface, E_A is the total energy of an isolated adsorbate in the gas phase, and $E_{(A+surf)}$ is the total energy of the surface with adsorbed species. The climbing-image nudged elastic band (CI-NEB) method was used for reaction barrier calculations.^{44,45}

3. RESULTS AND DISCUSSION

Figure 3 depicts the reduction profile of FeTiO₃ with CH₄ at temperatures ranging from 900 to 1000 °C. The reduction was performed until the start of a sudden increase in weight as a result of carbon deposition on the sample. Across all of the temperatures, the reduction profile depicts a sigmoidal profile, with a slow initial rate followed by an increase in the reaction rate and finally slowing before the reduction was stopped.

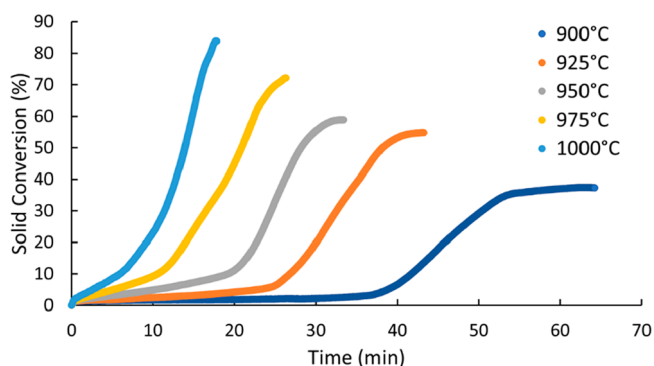


Figure 3. FeTiO₃ reduction with CH₄ at temperatures between 900 and 1000 °C and 1 atm in the TGA.

Moreover, increasing the temperature raises the reduction rate, with the sigmoidal curve being less pronounced at 1000 °C.

This reduction curve gives insight into the changes that occur on the FeTiO₃ sample as the reduction progresses. The slow reduction rate could be initially attributed to the lower rate of CH₄ activation on fully oxidized FeTiO₃. Because CH₄ reduces the oxygen carrier surface by abstracting lattice oxygen, the resulting oxygen vacancy is healed by outward or horizontal diffusion of lattice oxygen. However, as the oxygen carrier becomes reduced further, the oxygen diffusion rate decreases, giving rise to the formation of oxygen vacancy.⁴⁶ Once the oxygen vacancies form and are stable on the surface, they can act as active sites for CO formation, which, in turn, creates more oxygen vacancies, leading to a cascading effect. This sharp increase continues as FeTiO₃ reduces to metallic Fe, which also catalyzes the CH₄ decomposition. As lattice oxygen depletes from the sample, the reduced oxygen carrier becomes prone to carbon deposition. The onset of carbon deposition on the sample is signified by the slowdown of the rate of reduction, which is seen toward the end of the sigmoidal curve. As the reduction temperature increases, the lattice oxygen diffusion rate increases, thereby enhancing the solid conversion before the carbon deposition occurs.

To further analyze the sigmoidal curve portrayed by the CH₄ reduction of FeTiO₃ in the TGA, a differential bed reactor was employed. The differential bed reactor was run at 950 °C to represent the different aspects of the sigmoidal curve and provide insight about the product gas distribution as the reduction progresses. Figure 4 depicts the reaction profile of FeTiO₃ reduction under a constant flow of CH₄ at 950 °C. CH₄ conversion is plotted against time, as shown in Figure 4a, where the trend resembles the sigmoidal curve seen in Figure 3. CH₄ conversion is low up to ~15 min, after which the CH₄ conversion increases up to 40 min. After 40 min, the CH₄ conversion has a small increase, followed by the curve leveling off until the end of the run. Correspondingly, the product gas composition was also captured for this run, as shown in Figure 4b. During the low CH₄ conversion region (0–15 min), the majority of the product gas coming out was CO₂. As the CH₄ conversion increases, the concentration of syngas also increases with a simultaneous decrease in the CO₂ concentration. The CO concentration reached a maximum at the 20 min mark, followed by a gradual decrease to zero. In ~40 min, H₂ was the only product exiting the reactor.

Initially, CH₄ conversion is low as a result of the low activity of the FeTiO₃ surface that does not have enough oxygen vacancies, which agrees with the trend of the TGA reduction

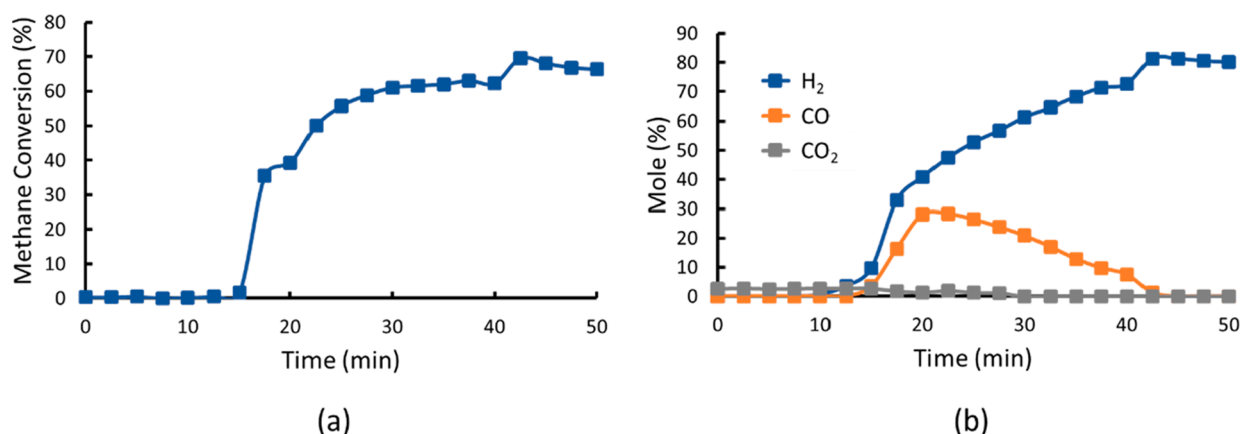


Figure 4. (a) CH₄ conversion plotted as a function of the reaction time and its corresponding (b) product composition as a function of the reaction time for the reduction of FeTiO₃ with CH₄ at 950 °C in a differential bed reactor.

curve. After 15 min, the surface of FeTiO₃ has stable oxygen vacancies, which results in the sharp increase in CH₄ reactivity. During this transition, the product composition shifts from producing combustion products, such as CO₂, to producing CO and H₂. This shift can be associated with the oxygen vacancy formation facilitating CH₄ dissociation.^{46–49} After 20 min, the CO concentration starts to drop but the H₂ concentration keeps increasing, which signifies the advent of carbon deposition on reduced FeTiO₃. From this point, the lattice oxygen diffusion in FeTiO₃ decreases with time, eventually going to zero. Thus, after ~42 min, CH₄ decomposes to carbon and H₂ on a completely reduced FeTiO₃ sample, which consists of metallic Fe and TiO₂. This differential bed test along with the TGA test indicates that the CH₄ dissociation is critically dependent upon the reducibility of FeTiO₃.

The CH₄–CO₂ co-feeding test was also conducted in the differential bed reactor. Five ratios of CH₄–CO₂ co-feed were investigated, which ranged from CH₄/CO₂ = 1 to 10, as seen in Figure 5. Because CH₄ and CO₂ are reducing and oxidizing

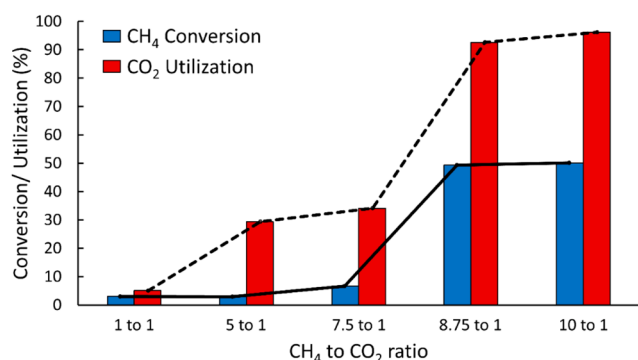


Figure 5. CH₄ conversion and CO₂ utilization over the FeTiO₃ oxygen carrier in a differential fixed bed reactor operated at different CH₄/CO₂ ratios at 950 °C and 1 atm.

gases, respectively, any composition of CH₄ and CO₂ created a dynamic kinetic equilibrium between the metal oxide reduction and oxidation. This equilibrium depends upon the composition of the co-feed gas. Figure 5 portrays the equilibrium performance under steady-state conditions for the different co-feed ratios. In these experiments, the CH₄ concentration in the feed was kept constant and the concentration of CO₂ was

decreased while maintaining the total flow rate at 100 mL/min by adding N₂. This was performed to maintain the residence time of the gas and keep a constant GHSV of CH₄ across all runs. As the CO₂ concentration drops in the co-feed mixture, both the CH₄ conversion and CO₂ reduction increase in a sigmoidal pattern. CH₄ conversion and CO₂ reduction show a lower performance up to a CH₄/CO₂ ratio of 7.5, after which the CH₄ conversion levels off at ~50% and the CO₂ reduction increases to >95%.

Because CH₄ conversion is a descriptor for oxygen vacancy formation on the surface, the plot in Figure 5 can be divided into two sections. The first section is from a CH₄/CO₂ ratio of 1 to 7.5. This section displays a lower performance, where the CH₄ conversion is low (<10%). The second section is from a CH₄/CO₂ ratio of 8.75 to 10, where the CH₄ conversion is relatively high. Interestingly, CO₂ reduction follows the same trend as CH₄ conversion, indicating that the CO₂ reduction is also critically dependent upon the reducibility of FeTiO₃.

The XRD spectra depict the phase composition of the post-reaction FeTiO₃ metal oxide samples from the five co-feed experiments at 950 °C, as seen in Figure 6a. In the low CH₄ conversion and CO₂ reduction section (CH₄/CO₂ = 1–7.5), the XRD shows FeTiO₃ as the dominant metal oxide phase. However, in the high CH₄ conversion and CO₂ reduction section (CH₄/CO₂ = 8.75–10), the XRD shows α-Fe, TiO₂, and carbon as the solid crystalline phase. The formation of carbon on the surface can also be observed from the Raman spectra of the samples, as shown in Figure 6b. The G and G' bands seen at wavelengths of 1580 and 2715 cm^{−1} for the CH₄/CO₂ ratio of 8.75–10 resemble graphitic carbon. An additional peak was seen at 2328 cm^{−1}. It corresponds to entrapped or adsorbed N₂, which was a common feature across all of the spectra.^{50,51} The abrupt change in phase with a relatively minor change in composition is consistent with the reactivity change that is seen with the differential bed tests in Figure 5.

To further analyze the samples, Mössbauer spectra was collected on these five samples post-reaction, as seen in Figure 6c. The objective with this technique was to use its fine resolution toward detecting changes in Fe coordination in the solid phase and give more insights than the XRD analysis. As seen from Figure 6c, metal oxides corresponding to the CH₄/CO₂ ratio of 1–7.5 co-feed composition show the formation of only the FeTiO₃ sextet.^{52,53} Because the CO₂ concentration was reduced in the case of the CH₄/CO₂ ratio of 8.75 and 10,

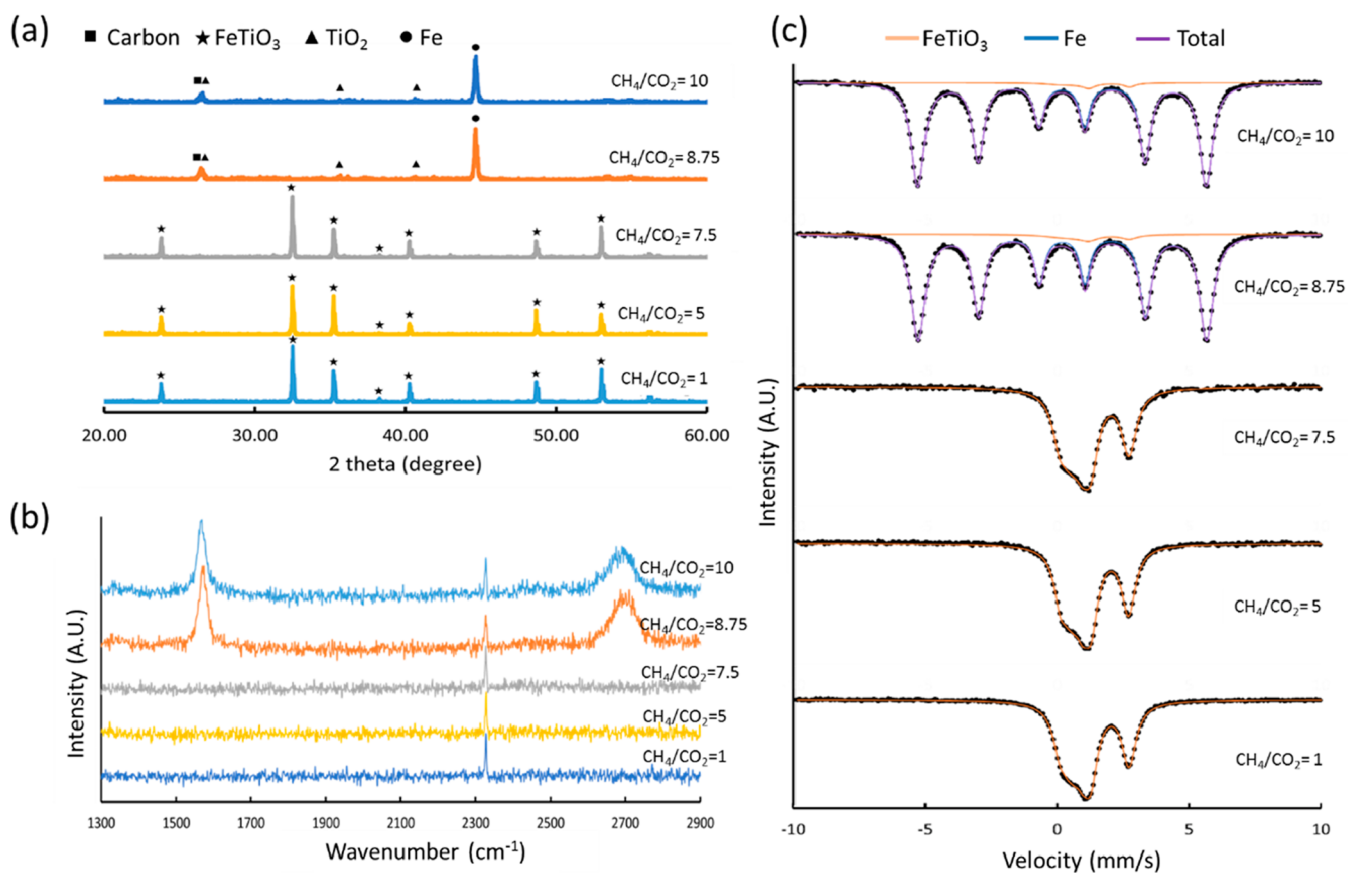


Figure 6. (a) XRD patterns, (b) Raman spectra, and (c) Mössbauer spectra of the co-feed samples for the CH_4/CO_2 ratio ranging from 1 to 10.

the spectra showed a α -Fe sextet with a small quantity of the FeTiO_3 sextet.⁵⁴ For the CH_4/CO_2 ratio of 8.75, FeTiO_3 was 4.56% of the total solid phase, and for the CH_4/CO_2 ratio of 10, FeTiO_3 was 3.33% of the total solid phase, with the balance being α -Fe in both of the cases. The phases seen in the Mössbauer spectra correlate well with the XRD spectra in Figure 6a. The Mössbauer spectra also indicated the presence of FeTiO_3 in the second section (CH_4/CO_2 ratio of 8.75–10). The difference of 1.23% between the two conditions corroborates well with the slight increase in the CO_2 utilization seen in Figure 5. The change in the gas composition from the CH_4/CO_2 ratio of 1 to 7.5 indicates an increase in the number of active sites on the oxygen carrier surface. However, because the phase does not change during the reaction, these active sites correspond to the oxygen vacancies in FeTiO_3 .

To gain mechanistic insight into CO_2 reduction with chemical looping reforming of methane, DFT calculations were performed to study the adsorption, activation, and dissociation of CO_2 and CH_4 on the FeTiO_3 surface. In FeTiO_3 , the Fe and Ti atoms are octahedrally coordinated to the oxygen atoms of hexagonally close-packed oxygen layers.^{55,56} According to this structure, the FeTiO_3 (0001) slab was modeled as shown in Figure 7a.

Because TGA and differential bed tests have indicated that CH_4 dissociation and CO_2 reduction are critically dependent upon the reducibility of FeTiO_3 , a reduced FeTiO_3 (0001) surface with various oxygen vacancies was modeled to investigate the surface interaction and possible elementary reactions. O_{3c} represents 3-fold bridging oxygen (O_{3c}). Removing O_{3c} causes the formation of an oxygen vacancy in

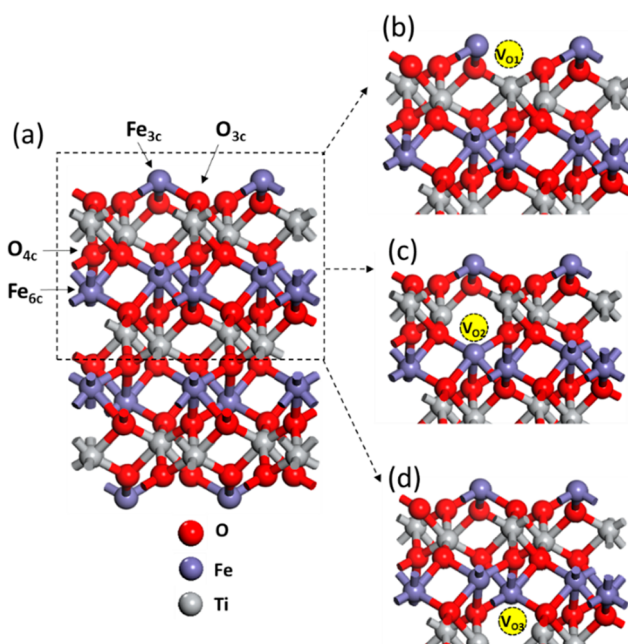


Figure 7. (a) Optimized structure of the FeTiO_3 (0001) surface and reduced FeTiO_3 (0001) surface with oxygen vacancy (b) $\text{V}_{\text{O}1}$, (c) $\text{V}_{\text{O}2}$, and (d) $\text{V}_{\text{O}3}$. Fe_{3c} and Fe_{6c} denote 3- and 6-fold coordinated Fe atom, respectively. O_{3c} and O_{4c} denote 3- and 4-fold coordinated oxygen atom, respectively.

the top surface ($\text{V}_{\text{O}1}$), as shown in Figure 7b. Similarly, $\text{V}_{\text{O}2}$ and $\text{V}_{\text{O}3}$ can be created by removing 4-fold bridging oxygen

(O_{4c}) in the subsurface, as shown in panels c and d of Figure 7, respectively. The formation energies for V_{O1}, V_{O2}, and V_{O3} are 236.29, 287.15, and 327.52 kJ/mol, respectively. Thus, the oxygen vacancies on the top surface V_{O1} are more stable than V_{O2} and V_{O3}, located in the subsurface of FeTiO₃. This results in the oxygen vacancy formation in the subsurface is more stable.⁵⁷

The optimized structures of CH₄ and CO₂ adsorbed on the FeTiO₃ (0001) surface and reduced surface with V_{O1} are shown in Figure 8a, and the relationship between their adsorption energies and the oxygen vacancy concentration are given in Figure 8b. CH₄ shows a weak interaction with the FeTiO₃ surface. However, the adsorption energy of the CO₂ molecule significantly increases upon the formation of oxygen

vacancies. For the stoichiometric FeTiO₃ (0001) surface, the most favorable configuration is found to be CO₂ adsorbed parallel between two Fe_{3c} atoms with an adsorption energy of 3.2 kJ/mol. For the reduced FeTiO₃ (0001) surface with the V_{O1} oxygen vacancy, the most favorable adsorption geometry consists of CO₂ adsorbed vertically to the surface at the oxygen vacancy site with an adsorption energy of 19.5 kJ/mol. Because the lowest unoccupied molecular orbital of a CO₂ molecule can accept electrons, a Bader charge analysis was performed on the FeTiO₃ (0001) surface with an adsorbed CO₂ molecule. The analysis shows that a charge of 0.785|e| transfers to the CO₂ molecule from the surface. However, the distance between the surface and adsorbed CO₂ is 2.229 Å, indicating that the charge transfer does not lead to the formation of carbonate species. Figure 8b shows that the adsorption energy of CO₂ increases to ~28 kJ/mol when the concentration of oxygen vacancies increases to ~7%.

Because CO₂ adsorption on the oxygen vacancy site is stronger than CH₄ adsorption, the oxygen vacancies created by the CH₄ reforming on the FeTiO₃ surface will be quickly occupied by CO₂ if the CH₄/CO₂ ratio is low. It results in a low CH₄ conversion as a result of the lack of active sites for CH₄ dissociation.⁵⁸ If the CH₄/CO₂ ratio is high, the surface will have enough oxygen vacancies for CH₄ dissociation, thus leading to a higher CH₄ conversion, which agrees with the plots in Figure 5.

CO₂ decomposition over the FeTiO₃ surface is promoted by adsorbed hydrogen atoms, which are from CH₄ dissociation, and the single O atom produced in this process may directly bind to the oxygen vacancy site, leading to oxygen vacancy healing.⁵⁹ In this study, three reaction pathways are proposed for the CO₂ decomposition: (i) direct reduction of CO₂ to CO, (ii) CO₂ hydrogenation to COOH* and then dissociation to CO, and (iii) CO₂ hydrogenation to HCOO* and then dissociation to CO. There is a large number of possible reaction steps during the CLR-CR reaction, which makes it difficult in determining the reaction mechanism. An energy barrier screening approach was applied to explore the favorable reaction path.⁴⁶ CH₃ is the first intermediate from CH₄ dissociation. The barrier analysis shows that CH₃ oxygenation to CH₃O needs to overcome a barrier of 137.62 kJ/mol. However, the energy barrier required for CH₃ dehydrogenation is only 108.15 kJ/mol. Therefore, CH₃ dehydrogenation to CH₂ is more favored than CH₃O formation on FeTiO₃. Similarly, in the step of CH* conversion, two possible paths were considered: CH* + O* → CHO* and CH* → C* + H*. The energy barrier calculations indicate that CH* from CH₂* decomposition prefers to further dissociate to the C radical (*E_a* = 106.38 kJ/mol) rather than abstracting one lattice oxygen atom from the surface (*E_a* = 154.19 kJ/mol). Therefore, the CH* → C* + H* path is chosen as the route to produce the next intermediate. The direct dissociation of CO₂ on FeTiO₃ was also investigated. It was found that the cleavage of the C–O bond of CO₂ to yield CO* + O* needs to overcome a barrier of 185.39 kJ/mol. It is much higher than that of CO₂ hydrogenation; thus, direct CO₂ decomposition on FeTiO₃ is kinetically inhibited. On the basis of this screening approach, the reaction network for CLR-CR is obtained as shown in Figure 9.

For the HCOO* (formate) route, the C–O bond of CO₂ is weakened by the addition of H, leading to the formation of HCO*, subsequently healing the oxygen vacancy. Considering that the hydrogenation barrier of HCO* is 115.75 kJ/mol, it

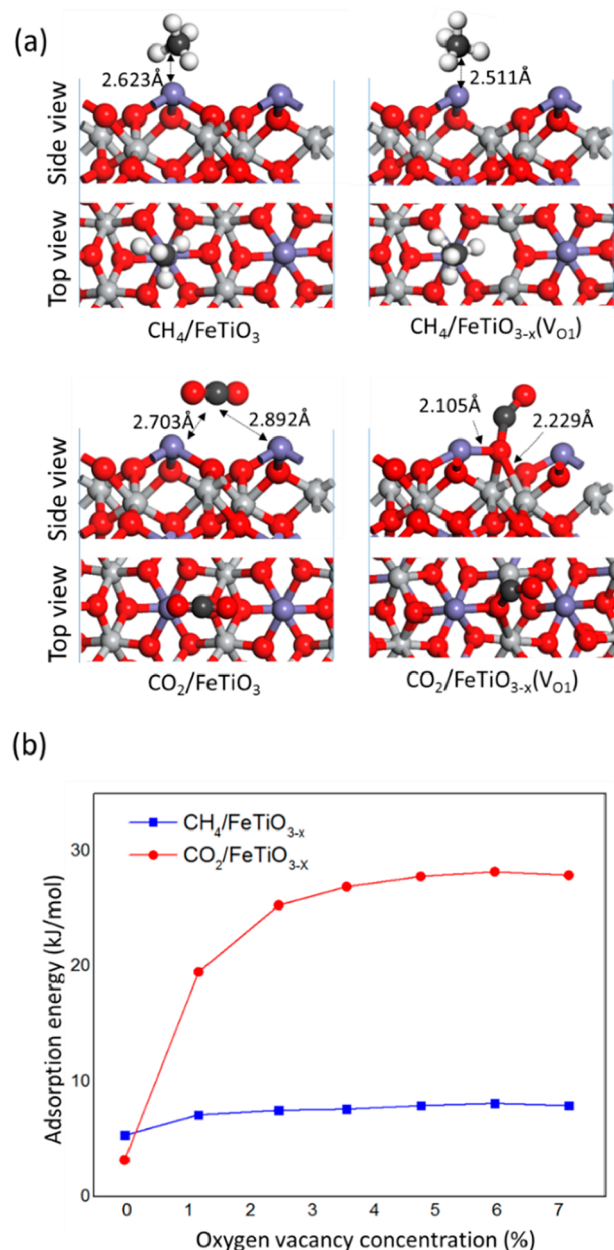


Figure 8. (a) Front view and top view of CH₄ and CO₂ adsorption on the FeTiO₃ (0001) surface and reduced surface with V_{O1} and (b) adsorption energy of CH₄ and CO₂ plotted as a function of the oxygen vacancy concentration.

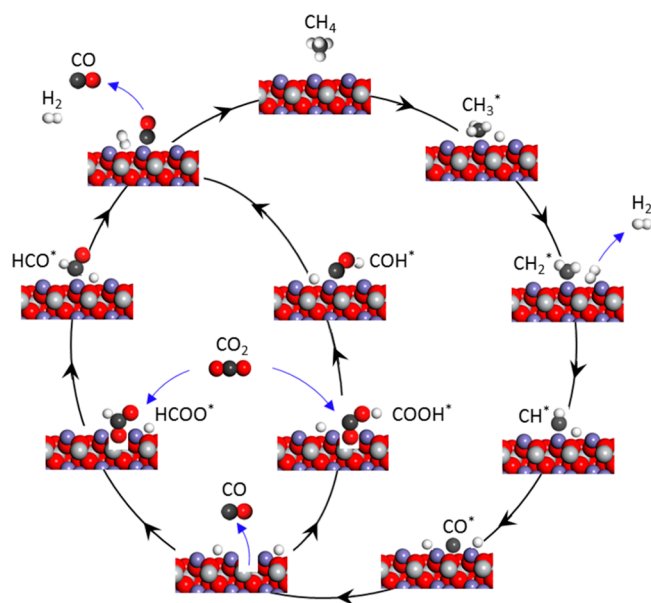


Figure 9. Proposed reaction scheme for the CLR-CR.

would prefer to undergo decomposition with a low barrier of 64.36 kJ/mol. For the step of CO_2 hydrogenation to HCOO^* , both the mono- HCOO^* and bi- HCOO^* have been considered. However, it was found that bi- HCOO^* is unstable as a result of the long distance between two surface Fe_{3c} sites. For the carboxylate route, the energy barrier required for the COOH^* formation is 102.17 kJ/mol, which is 45.32 kJ/mol higher than that of the HCOO^* formation in the formate route. It is attributed to the larger distance between the migrating hydrogen atom and the oxygen atom of CO_2 . The calculated energy profile of the CLR-CR is given in Figure 10. It shows that CH_4 dehydrogenation to CH_3 is the rate-limiting step with a barrier of 160.29 kJ/mol. Four hydrogen atoms will be generated after methane full dissociation. These hydrogen atoms promote CO_2 activation and conversion to the HCOO^* intermediates. Overall, the methane dissociation enhances the competitiveness of the HCOO^* formation to the COOH^* formation on reduced FeTiO_3 . Subsequently, higher CO_2

conversion is achieved with the fast decomposition of the HCOO^* intermediates at oxygen vacancy sites. Therefore, both the oxygen vacancies and hydrogen atoms are verified to be responsible for enhancing CO_2 reduction and can improve the reactivity of FeTiO_3 oxygen carriers in CLR-CR.

4. CONCLUSION

Chemical looping CH_4 reforming coupled with CO_2 reduction over ilmenite has been studied by combining redox experiments and DFT calculations. The thermogravimetric analysis on the reactivity of FeTiO_3 for CH_4 conversion showed a sigmoidal behavior across five temperatures between 900 and 1000 $^\circ\text{C}$, which was also confirmed by the differential bed test. At the CH_4/CO_2 ratios of 1–7.5, both the CH_4 and CO_2 conversions were low. However, increasing the CH_4/CO_2 ratio to 8.75 significantly improves the activity of FeTiO_3 , which achieves CO_2 reduction of $\sim 95\%$. It was found that the oxygen vacancies and hydrogen atoms from CH_4 are crucial to the activity of FeTiO_3 . The successive dissociation of CH_4 on FeTiO_3 results in the formation of oxygen vacancies. CO_2 prefers to be hydrogenated to the HCOO^* species at these oxygen vacancy sites rather than being hydrogenated to COOH^* or direct splitting to CO . It indicates that the formate pathway is the dominant mechanism for the CLR-CR. In this pathway, HCOO^* is converted to CO via the C–O and C–H cleavage at the oxygen vacancy site, with a low energy barrier of 62.5 kJ/mol. Therefore, the FeTiO_3 surface with a high concentration of oxygen vacancies and dissociative CH_4 is favorable for CO_2 conversion. The results indicate that the economical iron–titanium composite material can realize near 100% CO_2 reduction through the CLR-CR process and deepen the fundamental understanding of the role of oxygen vacancies on hydrogen-assisted CO_2 activation and reduction, which can be applied to design highly efficient oxygen carriers for CO_2 utilization in chemical looping systems.

AUTHOR INFORMATION

Corresponding Author

Zhuo Cheng – Department of Chemical and Biomolecular Engineering, The Ohio State University, Columbus, Ohio

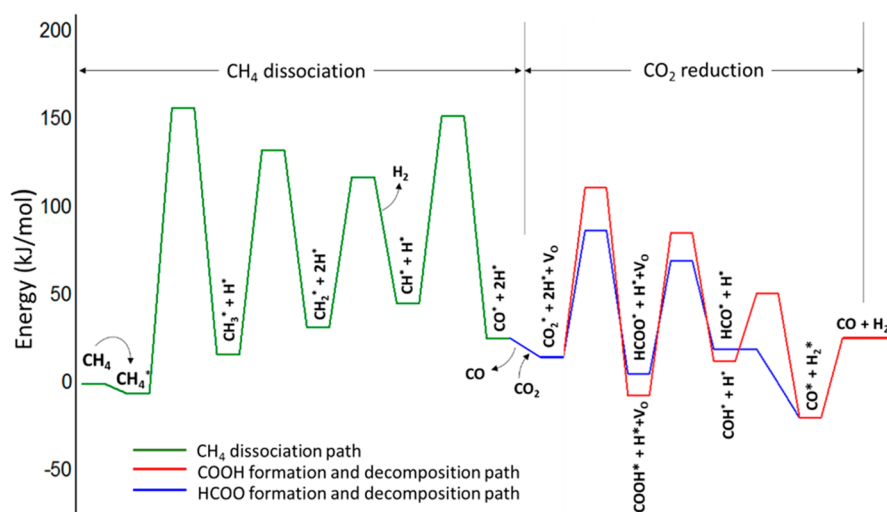


Figure 10. Energy profiles for CH_4 dissociation and CO_2 conversion during the CLR-CR.

43210, United States; orcid.org/0000-0001-7910-4264;
Email: cheng.963@osu.edu

Authors

Deven S. Baser – Department of Chemical and Biomolecular Engineering, The Ohio State University, Columbus, Ohio 43210, United States; orcid.org/0000-0003-2658-2451

Vedant Shah – Department of Chemical and Biomolecular Engineering, The Ohio State University, Columbus, Ohio 43210, United States

Jonathan A. Fan – Department of Electrical Engineering, Ginzton Laboratory, Spilker Engineering and Applied Sciences, Stanford University, Stanford, California 94305, United States; orcid.org/0000-0001-9816-9979

Liang-Shih Fan – Department of Chemical and Biomolecular Engineering, The Ohio State University, Columbus, Ohio 43210, United States

Complete contact information is available at:

<https://pubs.acs.org/10.1021/acs.energyfuels.0c03214>

Author Contributions

[†]Zhuo Cheng and Deven S. Baser contributed equally to this work.

Notes

The authors declare no competing financial interest.

ACKNOWLEDGMENTS

The service support provided by the Center for Electron Microscopy and the Analysis and the NanoSystem Laboratory at The Ohio State University and the computing support provided by the Ohio Supercomputer Center are gratefully acknowledged.

REFERENCES

- (1) Mardani, A.; Streimikiene, D.; Cavallaro, F.; Loganathan, N.; Khoshnoudi, M. Carbon Dioxide (CO₂) Emissions and Economic Growth: A Systematic Review of Two Decades of Research from 1995 to 2017. *Sci. Total Environ.* **2019**, *649*, 31–49.
- (2) Leung, D. Y. C.; Caramanna, G.; Maroto-Valer, M. M. An Overview of Current Status of Carbon Dioxide Capture and Storage Technologies. *Renewable Sustainable Energy Rev.* **2014**, *39*, 426–443.
- (3) Boot-Handford, M. E.; Abanades, J. C.; Anthony, E. J.; Blunt, M. J.; Brandani, S.; Mac Dowell, N.; Fernández, J. R.; Ferrari, M.-C.; Gross, R.; Hallett, J. P.; et al. Carbon Capture and Storage Update. *Energy Environ. Sci.* **2014**, *7* (1), 130–189.
- (4) Bui, M.; Adjiman, C. S.; Bardow, A.; Anthony, E. J.; Boston, A.; Brown, S.; Fennell, P. S.; Fuss, S.; Galindo, A.; Hackett, L. A.; et al. Carbon Capture and Storage (CCS): The Way Forward. *Energy Environ. Sci.* **2018**, *11* (5), 1062–1176.
- (5) MacDowell, N.; Florin, N.; Buchard, A.; Hallett, J.; Galindo, A.; Jackson, G.; Adjiman, C. S.; Williams, C. K.; Shah, N.; Fennell, P. An Overview of CO₂ Capture Technologies. *Energy Environ. Sci.* **2010**, *3* (11), 1645–1669.
- (6) Fan, L.-S. *Chemical Looping Partial Oxidation: Gasification, Reforming, and Chemical Syntheses*; Cambridge University Press: Cambridge, U.K., 2017; DOI: [10.1017/9781108157841](https://doi.org/10.1017/9781108157841).
- (7) Sanz-Pérez, E. S.; Murdock, C. R.; Didas, S. A.; Jones, C. W. Direct Capture of CO₂ from Ambient Air. *Chem. Rev.* **2016**, *116* (19), 11840–11876.
- (8) Kumar, A.; Madden, D. G.; Lusi, M.; Chen, K.-J.; Daniels, E. A.; Curtin, T.; Perry, J. J., IV; Zaworotko, M. J. Direct Air Capture of CO₂ by Physisorbent Materials. *Angew. Chem., Int. Ed.* **2015**, *54* (48), 14372–14377.
- (9) Rafiee, A.; Rajab Khalilpour, K.; Milani, D.; Panahi, M. Trends in CO₂ Conversion and Utilization: A Review from Process Systems Perspective. *J. Environ. Chem. Eng.* **2018**, *6* (5), 5771–5794.
- (10) Artz, J.; Müller, T. E.; Thenert, K.; Kleinekorte, J.; Meys, R.; Sternberg, A.; Bardow, A.; Leitner, W. Sustainable Conversion of Carbon Dioxide: An Integrated Review of Catalysis and Life Cycle Assessment. *Chem. Rev.* **2018**, *118* (2), 434–504.
- (11) Benson, E. E.; Kubiak, C. P.; Sathrum, A. J.; Smieja, J. M. Electrocatalytic and Homogeneous Approaches to Conversion of CO₂ to Liquid Fuels. *Chem. Soc. Rev.* **2009**, *38* (1), 89–99.
- (12) Zheng, Y.; Zhang, W.; Li, Y.; Chen, J.; Yu, B.; Wang, J.; Zhang, L.; Zhang, J. Energy Related CO₂ Conversion and Utilization: Advanced Materials/Nanomaterials, Reaction Mechanisms and Technologies. *Nano Energy* **2017**, *40*, 512–539.
- (13) Castro, S.; Albo, J.; Irabien, A. Photoelectrochemical Reactors for CO₂ Utilization. *ACS Sustainable Chem. Eng.* **2018**, *6* (12), 15877–15894.
- (14) Molitor, H. R.; Moore, E. J.; Schnoor, J. L. Maximum CO₂ Utilization by Nutritious Microalgae. *ACS Sustainable Chem. Eng.* **2019**, *7* (10), 9474–9479.
- (15) Wang, W.; Wang, Y.; Li, C.; Yan, L.; Jiang, M.; Ding, Y. State-of-the-Art Multifunctional Heterogeneous POP Catalyst for Cooperative Transformation of CO₂ to Cyclic Carbonates. *ACS Sustainable Chem. Eng.* **2017**, *5* (6), 4523–4528.
- (16) Meng, X.; He, H.; Nie, Y.; Zhang, X.; Zhang, S.; Wang, J. Temperature-Controlled Reaction–Separation for Conversion of CO₂ to Carbonates with Functional Ionic Liquids Catalyst. *ACS Sustainable Chem. Eng.* **2017**, *5* (4), 3081–3086.
- (17) Pakhare, D.; Spivey, J. A Review of Dry (CO₂) Reforming of Methane over Noble Metal Catalysts. *Chem. Soc. Rev.* **2014**, *43* (22), 7813–7837.
- (18) Muraza, O.; Galadima, A. A Review on Coke Management during Dry Reforming of Methane. *Int. J. Energy Res.* **2015**, *39* (9), 1196–1216.
- (19) Arora, S.; Prasad, R. An Overview on Dry Reforming of Methane: Strategies to Reduce Carbonaceous Deactivation of Catalysts. *RSC Adv.* **2016**, *6* (110), 108668–108688.
- (20) Zhang, P.; Tong, J.; Huang, K. Combining Electrochemical CO₂ Capture with Catalytic Dry Methane Reforming in a Single Reactor for Low-Cost Syngas Production. *ACS Sustainable Chem. Eng.* **2016**, *4* (12), 7056–7065.
- (21) Buelens, L. C.; Galvita, V. V.; Poelman, H.; Detavernier, C.; Marin, G. B. Super-Dry Reforming of Methane Intensifies CO₂ Utilization via Le Chatelier's Principle. *Science* **2016**, *354* (6311), 449–452.
- (22) Kathe, M.; Empfield, A.; Sandvik, P.; Fryer, C.; Zhang, Y.; Blair, E.; Fan, L.-S. Utilization of CO₂ as a Partial Substitute for Methane Feedstock in Chemical Looping Methane–Steam Redox Processes for Syngas Production. *Energy Environ. Sci.* **2017**, *10* (6), 1345–1349.
- (23) Baser, D. S.; Nadgouda, S. G.; Joshi, A. S.; Fan, L.-S. 110th Anniversary: Indirect Partial Oxidation of Methane Using a Counter-Current Moving-Bed Chemical Looping Configuration for Enhanced Syngas Production. *Ind. Eng. Chem. Res.* **2019**, *58* (36), 16407–16416.
- (24) Hu, J.; Galvita, V. V.; Poelman, H.; Marin, G. B. Advanced Chemical Looping Materials for CO₂ Utilization: A Review. *Materials* **2018**, *11* (7), 1187.
- (25) Fan, L.-S. *Chemical Looping Systems for Fossil Energy Conversions*; John Wiley & Sons: Hoboken, NJ, 2011.
- (26) Najera, M.; Solunke, R.; Gardner, T.; Vesper, G. Carbon Capture and Utilization via Chemical Looping Dry Reforming. *Chem. Eng. Res. Des.* **2011**, *89* (9), 1533–1543.
- (27) Haribal, V. P.; Wang, X.; Dudek, R.; Paulus, C.; Turk, B.; Gupta, R.; Li, F. Modified Ceria for “Low-Temperature” CO₂ Utilization: A Chemical Looping Route to Exploit Industrial Waste Heat. *Adv. Energy Mater.* **2019**, *9* (41), 1901963.
- (28) Tian, S.; Yan, F.; Zhang, Z.; Jiang, J. Calcium-Looping Reforming of Methane Realizes in Situ CO₂ Utilization with Improved Energy Efficiency. *Sci. Adv.* **2019**, *5* (4), eaav5077.

- (29) Galvita, V. V.; Poelman, H.; Bliznuk, V.; Detavernier, C.; Marin, G. B. CeO_2 -Modified Fe_2O_3 for CO_2 Utilization via Chemical Looping. *Ind. Eng. Chem. Res.* **2013**, *52* (25), 8416–8426.
- (30) Kathe, M.; Sandvik, P.; Fryer, C.; Kong, F.; Zhang, Y.; Grigoris, G.; Fan, L.-S. Coal Refining Chemical Looping Systems with CO_2 as a Co-Feedstock for Chemical Syntheses. *Energy Fuels* **2018**, *32* (2), 1139–1154.
- (31) Kathe, M.; Fryer, C.; Sandvik, P.; Kong, F.; Zhang, Y.; Empfield, A.; Fan, L.-S. Modularization Strategy for Syngas Generation in Chemical Looping Methane Reforming Systems with CO_2 as Feedstock. *AIChE J.* **2017**, *63* (8), 3343–3360.
- (32) Luo, S.; Zeng, L.; Xu, D.; Kathe, M.; Chung, E.; Deshpande, N.; Qin, L.; Majumder, A.; Hsieh, T.-L.; Tong, A.; et al. Shale Gas-to-Syngas Chemical Looping Process for Stable Shale Gas Conversion to High Purity Syngas with a H_2 : CO Ratio of 2:1. *Energy Environ. Sci.* **2014**, *7* (12), 4104–4117.
- (33) Chung, E. Y.; Wang, W. K.; Nadgouda, S. G.; Baser, D. S.; Sofranko, J. A.; Fan, L.-S. Catalytic Oxygen Carriers and Process Systems for Oxidative Coupling of Methane Using the Chemical Looping Technology. *Ind. Eng. Chem. Res.* **2016**, *55* (50), 12750–12764.
- (34) Cheng, Z.; Baser, D. S.; Nadgouda, S. G.; Qin, L.; Fan, J. A.; Fan, L.-S. C_2 Selectivity Enhancement in Chemical Looping Oxidative Coupling of Methane over a Mg–Mn Composite Oxygen Carrier by Li-Doping-Induced Oxygen Vacancies. *ACS Energy Lett.* **2018**, *3* (7), 1730–1736.
- (35) Kresse, G.; Furthmüller, J. Efficiency of Ab-Initio Total Energy Calculations for Metals and Semiconductors Using a Plane-Wave Basis Set. *Comput. Mater. Sci.* **1996**, *6* (1), 15–50.
- (36) Kresse, G.; Hafner, J. Ab Initio Molecular Dynamics for Liquid Metals. *Phys. Rev. B: Condens. Matter Mater. Phys.* **1993**, *47* (1), 558–561.
- (37) Kresse, G.; Furthmüller, J. Efficient Iterative Schemes for Ab Initio Total-Energy Calculations Using a Plane-Wave Basis Set. *Phys. Rev. B: Condens. Matter Mater. Phys.* **1996**, *54* (16), 11169–11186.
- (38) Perdew, J. P.; Burke, K.; Ernzerhof, M. Generalized Gradient Approximation Made Simple. *Phys. Rev. Lett.* **1996**, *77* (18), 3865–3868.
- (39) Blöchl, P. E. Projector Augmented-Wave Method. *Phys. Rev. B: Condens. Matter Mater. Phys.* **1994**, *50* (24), 17953–17979.
- (40) Kresse, G.; Joubert, D. From ultrasoft pseudopotentials to the projector augmented-wave method. *Phys. Rev. B: Condens. Matter Mater. Phys.* **1999**, *59* (3), 1758–1775.
- (41) Blöchl, P. E.; Jepsen, O.; Andersen, O. K. Improved Tetrahedron Method for Brillouin-Zone Integrations. *Phys. Rev. B: Condens. Matter Mater. Phys.* **1994**, *49* (23), 16223–16233.
- (42) Herbst, J. F.; Watson, R. E.; Wilkins, J. W. Relativistic Calculations of $4f$ Excitation Energies in the Rare-Earth Metals: Further Results. *Phys. Rev. B: Condens. Matter Mater. Phys.* **1978**, *17* (8), 3089–3098.
- (43) Anisimov, V. I.; Gunnarsson, O. Density-Functional Calculation of Effective Coulomb Interactions in Metals. *Phys. Rev. B: Condens. Matter Mater. Phys.* **1991**, *43* (10), 7570–7574.
- (44) Henkelman, G.; Uberuaga, B. P.; Jónsson, H. A Climbing Image Nudged Elastic Band Method for Finding Saddle Points and Minimum Energy Paths. *J. Chem. Phys.* **2000**, *113*, 9901–9904.
- (45) Henkelman, G.; Jónsson, H. Improved Tangent Estimate in the Nudged Elastic Band Method for Finding Minimum Energy Paths and Saddle Points. *J. Chem. Phys.* **2000**, *113*, 9978–9985.
- (46) Cheng, Z.; Qin, L.; Guo, M.; Xu, M.; Fan, J. A.; Fan, L.-S. Oxygen Vacancy Promoted Methane Partial Oxidation over Iron Oxide Oxygen Carriers in the Chemical Looping Process. *Phys. Chem. Chem. Phys.* **2016**, *18* (47), 32418–32428.
- (47) Guo, M.; Cheng, Z.; Liu, Y.; Qin, L.; Goetze, J.; Fan, J. A.; Fan, L.-S. Cobalt Doping Modification for Enhanced Methane Conversion at Low Temperature in Chemical Looping Reforming Systems. *Catal. Today* **2020**, *350*, 156–164.
- (48) Cheng, Z.; Qin, L.; Guo, M.; Fan, J. A.; Xu, D.; Fan, L.-S. Methane Adsorption and Dissociation on Iron Oxide Oxygen Carriers: The Role of Oxygen Vacancies. *Phys. Chem. Chem. Phys.* **2016**, *18* (24), 16423–16435.
- (49) Qin, L.; Guo, M.; Liu, Y.; Cheng, Z.; Fan, J. A.; Fan, L.-S. Enhanced Methane Conversion in Chemical Looping Partial Oxidation Systems Using a Copper Doping Modification. *Appl. Catal., B* **2018**, *235*, 143–149.
- (50) Dhakal, A.; Wuytens, P.; Raza, A.; Le Thomas, N.; Baets, R. Silicon Nitride Background in Nanophotonic Waveguide Enhanced Raman Spectroscopy. *Materials* **2017**, *10* (2), 140.
- (51) Pimenta, M. A.; Dresselhaus, G.; Dresselhaus, M. S.; Cancado, L. G.; Jorio, A.; Saito, R. Studying Disorder in Graphite-Based Systems by Raman Spectroscopy. *Phys. Chem. Chem. Phys.* **2007**, *9* (11), 1276–1290.
- (52) Van Alboom, A.; De Grave, E. Temperature Dependences of the Hyperfine Parameters of Fe^{2+} in FeTiO_3 as Determined by ^{57}Fe -Mössbauer Spectroscopy. *Am. Mineral.* **2016**, *101* (3), 735–743.
- (53) Grant, R. W.; Housley, R. M.; Geller, S. Hyperfine Interactions of Fe^{2+} in Ilmenite. *Phys. Rev. B* **1972**, *5* (5), 1700–1703.
- (54) Channing, D. A.; Graham, M. J. A Study of Iron Oxidation Processes by Mössbauer Spectroscopy. *Corros. Sci.* **1972**, *12* (3), 271–289.
- (55) Wilson, N. C.; Muscat, J.; Mkhonto, D.; Ngoepe, P. E.; Harrison, N. M. Structure and Properties of Ilmenite from First Principles. *Phys. Rev. B: Condens. Matter Mater. Phys.* **2005**, *71* (7), 75202.
- (56) Fellows, R. A.; Lennie, A. R.; Vaughan, D. J.; Thornton, G. A LEED Study of the FeTiO_3 (0001) Surface Following Annealing in O_2 Partial Pressures. *Surf. Sci.* **1997**, *383* (1), 50–56.
- (57) Wang, Y.; Sun, H.; Tan, S.; Feng, H.; Cheng, Z.; Zhao, J.; Zhao, A.; Wang, B.; Luo, Y.; Yang, J.; et al. Role of Point Defects on the Reactivity of Reconstructed Anatase Titanium Dioxide (001) Surface. *Nat. Commun.* **2013**, *4*, 2214.
- (58) Zeng, L.; Cheng, Z.; Fan, J. A.; Fan, L.-S.; Gong, J. Metal Oxide Redox Chemistry for Chemical Looping Processes. *Nat. Rev. Chem.* **2018**, *2* (11), 349–364.
- (59) Cheng, Z.; Sherman, B. J.; Lo, C. S. Carbon Dioxide Activation and Dissociation on Ceria (110): A Density Functional Theory Study. *J. Chem. Phys.* **2013**, *138* (1), 014702.